Optical turbulence on 1 km horizontal path with short and medium infrared laser beams

Andreas Schiller[a], Helge Fonnum[a], and Espen Lippert[a]

[a]Norwegian Defence Research Establishment (FFI), Instituttveien 20, 2007 Kjeller, Norway

ABSTRACT

We have investigated effects of optical turbulence on laser beams with wavelengths of $\lambda = 1064$ nm and 2036 nm. The two laser beams (one diode and one thulium fiber laser) were expanded to 7 cm diameter through a common telescope by means of an off-axis parabolic mirror. The two approximately Gaussian beams were focused along a 1 km long horizontal path (about 1 m above ground) onto a roughened metal plate. The beam spots were recorded by two separate cameras with band-pass filters. The laser beams were pulsed at 50 Hz and synchronized with the camera shutters. Altogether 76 runs of 20 s length (resulting in 1000 single frames each) were recorded during the days of Oct. 12–14, 2022 at ONERAs test site in Fauga-Mauzac in southern France. Turbulence conditions during that time varied from C_n^2 as low as a few 10^{-16} m$^{-2/3}$ to as high as several 10^{-13} m$^{-2/3}$. We discuss our findings for both wavelengths in terms of long-term (20 s) beam spot size, short-term (fraction of ms) beam spot size as well as spatial and temporal beam wander. We also find departure from Gaussian beam shape in average at increasing turbulence level. Comparison of experimental data with some selected models is provided.

Keywords: Optical turbulence, laser beam, stochastic process

1. INTRODUCTION

The Norwegian Defence Research Establishment (FFI) has a goal to produce a kW laser at 2 μm wavelength and to deliver a sizeable portion of this laser effect over distance onto a potentially fast moving target. A prototype demonstrator at some intermediate technical readiness level (TRL) is in planning for the year 2025. In this context, FFI aims to raise general in-house competency and experience with laser propagation through atmosphere. Furthermore some specific questions about fine-tracking of a target have emerged which have connections with laser propagation through turbulent atmosphere. The overarching question is about the best strategy to deliver sufficient energy on a given spot on the target such that it takes damage. In more detail, we are interested in (i) the long-term, average beam spot size (ii) the degree of beam wander (its size and frequency content) i.e., the contribution to the beam spot size which might be counteracted by a sufficiently fast tip-tilt mechanism (iii) the turbulence level at which point the beam breaks up into two or more distinct spotlets – an effect which might confuse an automatic fine tracker and (iv) the average short-term beam spot size, i.e., the contribution to the beam spot size which can only be counteracted by adaptive optics. In order to address some of these questions, FFI joined the NATO Sensors and Electronic Technology SET-304 TG technical group. This technical group arranged a field trial in mid October 2022 in southern France (near Toulouse, hosted by ONERA – the French Aerospace Lab), where participating institutions could run experiments under turbulence conditions which were closely monitored by, among others, a scintillometer, a weather station and temperature gradient measurements. FFI contributed with two lasers with 1 and 2 μm wavelength sharing a common beam axis and with cameras to monitor the beam spots. Here, some of the key findings of this experiment are presented. In Section 2, the experimental setup is described in detail, then, in Section 3, the data taking, some intial data processing and first impressions from the data images are discussed. Section 4 describes the mathematical framework for further data processing while Sections 5 and 6 discuss our findings on beam wander and spot size, respectively. The conclusions and an outlook on future work are given in Section 7.

Further author information: (Send correspondence to A. Schiller)
A. Schiller: E-mail: Andreas-Ulrich.Schiller@ffi.no, Telephone: +47 45623824

Environmental Effects on Light Propagation and Adaptive Systems VI, edited by Karin Stein, Szymon Gladysz, Proc. of SPIE Vol. 12731, 127310A
 · 0277-786X · doi: 10.1117/12.2678536

2. EXPERIMENT

The experimental setup consists of a laser head, where two laser beams of 1 μm and 2 μm wavelength are combined (in the sense that they share a common beam axis) and expanded from their 7 mm diameter by a factor of 10 through a common telescope. The telescope is also used to focus the beams onto a metal plate with a roughened surface at some 1 km distance. The path of the laser beam lies roughly 1 m above ground. The beam spots of the laser beams are observed and recorded by two cameras at short distance from the metal plate, each of which sensitive to one of the wavelengths and equipped with a bandpass filter to improve the signal-to-noise ratio. The schematic of the setup is shown in Figure 1.

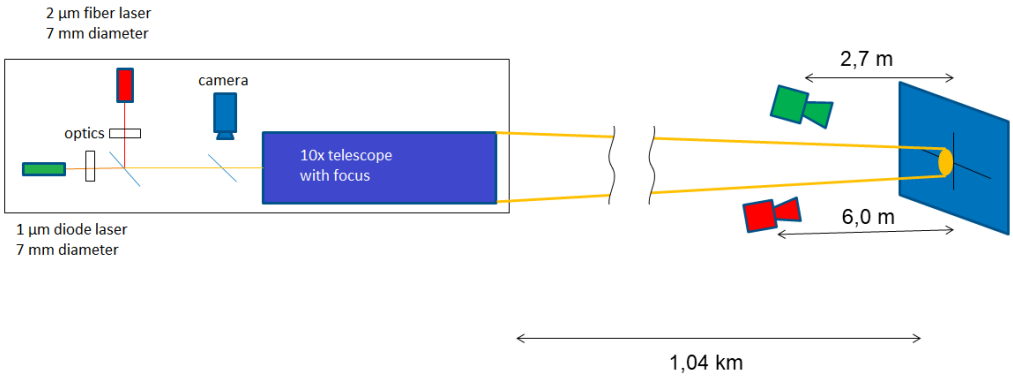

Figure 1. Schematic of the setup. The laser head consists of the laser sources, a telescope and related optics to produce two co-linear beams of 7 cm diameter focused on a target at the far end of the 1 km test lane. A camera in the laser head can be used to image the target through the telescope. On the receiver end, two cameras observe and record the beam spots off a roughened metal sheet.

Specifically, the 1 μm or SWIR (short-wavelength infrared) laser consists of a fiber-coupled 1064 nm DFB (distributed feedback) laser and collimater (marked KO1 in Figure 2). This laser produces 20 mW effect and is collimated to a 7 mm ($1/e^2$) diameter beam. The collimated beam can be focused by a 1:1 focusing telescope (marked T1 in Figure 2). The 2 μm or MWIR (mid-wavelength infrared) laser consists of a 2036 nm thulium fiber laser and collimator (marked KO2 in Figure 2). This laser produces 3 W effect and is collimated to a 4,3 mm diameter beam. Since we would like to reduce this effect down to 250 mW for safety reasons, but the laser source is not stable at such a low effect, the beam is reflected off a CaF_2 wedge (marked KI2 in Figure 2) at such an angle that only the desired fraction of the laser effect makes it into the next optical element. The collimated and effect-reduced beam can be focused by a 10:16 focussing telescope (marked T2 in Figure 2) and is expanded by it to the same 7 mm diameter as the 1 μm beam. Both beams are combined by means of a plate which is transparent for 1 μm light but highly reflective for 2 μm light (marked SK in Figure 2). The combined beams pass a second CaF_2 wedge (marked KI1 in Figure 2) which allows a camera (marked KA in Figure 2) to view the target through the same telescope. The camera with its lens has a focal length of 200 mm, however, together with the telescope, the effective focal length becomes 2 m. This, together with the camera's sensor area reduces its field-of-view to less than 4 mrad.

The telescope or $\times 10$ beam expander is marked SF in Figure 2 and is an off-axis beam expander (COAR series) by the company SORL (Space Optics Research Labs LLC) of the type SORL COAR 10$\times$ 10 Q, which means that it expands by a factor of 10 and accepts collimated beams of an input diameter of up to 10 mm and that the mirror surface is of high quality ($\lambda/10$ for the primary mirror and $\lambda/5$ for the secondary one). It is an off-axis achromatic beam expander with an ultra-low thermal expansion ceramic primary mirror. All elements are coated to provide 96% average system transmission (all specifications according to[1]). In the absence of optical turbulence and with a laser beam quality corresponding to $M^2 = 1$, the telescope should be able to produce beam spots on the 1 km distant target with a radius of 1 cm and 2 cm for the 1 μm and 2 μm laser beams, respectively.

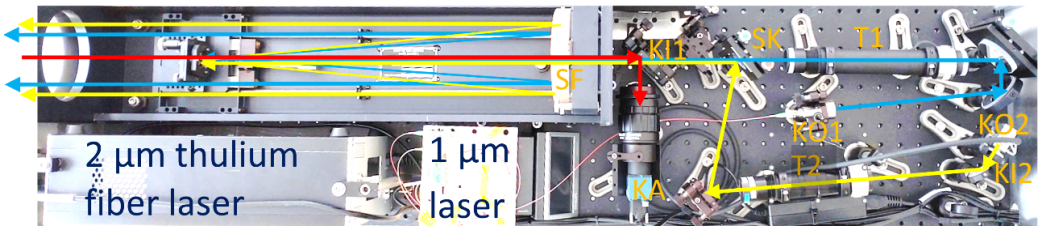

Figure 2. Details of the laser head. The path of the 1 μm laser light is marked by blue arrows, the path of the 2 μm light is marked by yellow arrows. Entering visual light for viewing the target is marked by red arrows. For details of the setup, see text.

In order for the setup to satisfy the requirements of laser safety class 1, but still produce beam spots with useable signal-to-noise ratio, the lasers were operated in a pulsed mode (for details see[2]). For this purpose, we chose pulse lengths of 750 μs with a repetition rate of 50 Hz. Since the peak effects were 20 mW and 250 mW for the 1 μm and 2 μm lasers, respectively, the average effects amounted to as little as 0,75 mW and 9,4 mW, respectively. Pulsed operation requires synchronization with the cameras which was achieved by using GPS (global positioning system) pulse-per-second signals. On both ends of the 1 km test lane, GPS signal receivers were coupled to FPGA (field-programmable gate array) cards in National Instrument CompactRIO units[3]. The FPGAs were programmed such that they generated pulse trains off the GPS pulses which drove the lasers and the cameras – each on their ends of the test lane. The pulse trains were adjusted to the GPS time at every full second in order to compensate for possible drifts in the FPGAs' internal clocks. A time stamp was produced each time a run with camera recordings was started.

The target was placed inside a small garage which was painted black on the inside in order to minimize the amount of indirect or reflected sunlight on the target. The spot produced by the 1 μm laser light was imaged by an InGaAs camera by the company Sensors Unlimited,[4] while the spot of the 2 μm laser light was imaged by an InSb camera by the company Teledyne FLIR.[5] The InGaAs camera is sensitive to a rather wide range of wavelengths – from 0,9 to 1,7 μm. In order to improve the signal-to-noise ratio, a narrow, 5 nm-wide bandpass filter was mounted. The camera has a focal length of 50 mm. It was placed at a distance of 2,7 m from the target. Since its pixel pitch is 25 μm, a pixel represents a square with a 1,3 mm edge on the target. The filter in front of the InSb camera was a bit more wide-band with a transmission window between 1900 nm and 2300 nm. The camera has a focal length of 100 mm and was mounted at a distance of 6,0 m from the target. Since its pixel pitch is only 15 μm, a pixel represents a square with an 0,87 mm edge on the target. The shutter time of both cameras was varied throughout the day in order to avoid saturation of pixels due to ambient sunlight and at low turbulence conditions. However, the maximum shutter time was limited to 750 μs due to the length of the laser pulses. Both cameras operated with a repetition rate of 100 Hz, which means that only every second frame recorded a laser beam. Every other frame was therefore a background image used for background subtraction.

3. DATA

Data taking happened in 76 20-s runs during the days of 12–14 of October, 2022 at ONERA's test site in Fauga-Mauzac near Toulouse in southern France. For every run, both of the cameras registered some 2000 single frames each, which were transfered to an external harddrive. The 1 μm camera recorded frames of the size 256 $\times$ 256 pixels (translating to a 33 cm $\times$ 33 cm patch on the target) with a 12 bit resolution of the intensity, thus allowing a maximum pixel value of 4 095. The 2 μm camera recorded frames of the size 640 $\times$ 512 pixels (translating to a 56 cm $\times$ 45 cm patch on the target) with a 14 bit resolution of the intensity, allowing a maximum pixel value of 16 383.

In the first step of the analysis, pairs of immediately following frames were identified, where one frame shows a beam photo while the other shows a background photo. From every such a pair, a background-subtracted frame was generated. This procedure revealed that the 1 μm camera dropped in average 16 frames per run in an apparently random fashion. This will become important later on, when we discuss temporal correlations between the fluctuations of the two laser beams. We also checked the number of saturated pixels (pixels that record the

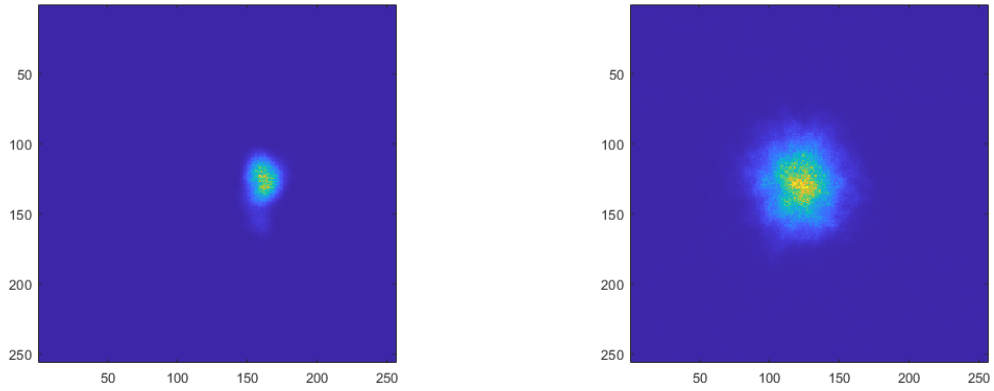

Figure 3. Video 1, 2. Average (over 20 s) background subtracted images and videos of the 1 μm laser beam for two runs, one at low turbulence conditions (left panel) and one at high turbulence conditions (right panel). For more details, see text. http://dx.doi.org/10.1117/12.2678536.1 http://dx.doi.org/10.1117/12.2678536.2

maximum possible intensity) *before* background subtraction and found that this concerned only a fraction of $10^{-6} - 10^{-7}$ of all the pixels in all the frames of all the runs.

For two of the runs (one with low and one with high turbulence conditions), we produced short videos from the background-subtracted single frames for both cameras. Figure 3 shows the average (over 20 s) background-subtracted images from run 30 (Oct. 12 at 19:04 with $C_n^2 \approx 1,1 \times 10^{-14}$ m$^{-2/3}$) and from run 50 (Oct. 13 at 14:50 with $C_n^2 \approx 1,2 \times 10^{-13}$ m$^{-2/3}$) recorded by the 1 μm camera. The value of the structure constant C_n^2 is based on ONERA's (uncorrected) scintillometer reading and was communicated to us by their staff. Links to the videos are contained in the figure caption. Figure 4 shows similar average background-subtracted images and videos (linked in the caption) from the same two runs but recorded by the 2 μm camera.

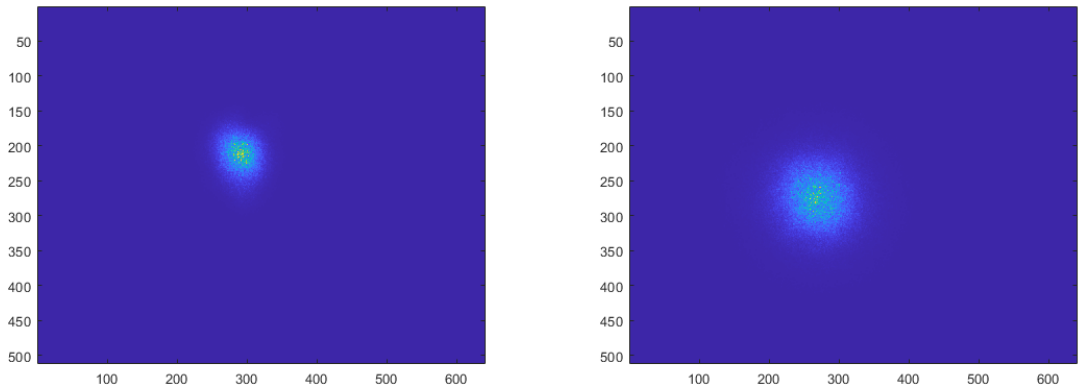

Figure 4. Video 3, 4. Average (over 20 s) background subtracted images and videos of the 2 μm laser beam for two runs, one at low turbulence conditions (left panel) and one at high turbulence conditions (right panel). For more details, see text. http://dx.doi.org/10.1117/12.2678536.3 http://dx.doi.org/10.1117/12.2678536.4

Already at this point, we can make a few interesting observations. On the left panel in Figure 3, one can see that the average beam spot is somewhat oblong and that there is a weak "shadow" below it. We will later see that for many of the runs up to run 64, the 1 μm (short-term) beamspot is indeed oblong, a fact which was obscured by beam wander, i.e., the beam spot moving around on the target in a random fashion and by optical turbulence in general. When the oblong shape of the 1 μm beamspot was discovered, it was corrected by small

adjustements of the optics in the laser head (see Figure 2). However, this adjustment made the 2 μm beam spot oblong for the remaining 12 runs – with the direction of its deformation axis almost perpendicular to the former deformation axis of the 1 μm beam spot. We will discuss this more in Section 6. The origin of the "shadow" below the average beam spot is clearly evident from watching the movie. For a few frames toward the end of the run, the beam spot dips by about 20 pixels, i.e., 2,5 cm for then to return to its original place. This is most likely caused by a relatively large eddy of air with a sizeable temperature gradient moving through the path of the laser light. We will come back to this point during the discussion of beam wander in Section 5. Comparing Figures 3 and 4, one can see that the average beam spot of the 1 μm laser seems to increase more with increasing turbulence than the one of the 2 μm laser. This is however somewhat deceiving, since we will show in Section 6, that we were not able to produce a diffraction-limited beam spot for the 2 μm laser. In terms of area, even at the lowest observed turbulence level, the recorded beam spot size is more than 2,5 times the theoretical limit. The final observation concerns the movies, where one can see that the beam spots at low turbulence level may deform somewhat and amble around, while at high turbulence level, they tend to break up into several fragments with the indivdual pieces dancing around the screen rather quickly. This qualitative difference in movement is definitively not apparent from the average images.

In order to characterize the beams, moments of the intensity distribution (in terms of pixel values) are calculated. For this purpose, it is essential that on the one hand, the entire beam is captured and on the other hand, no background intensity is remaining. Moreover, in case of small beam spots, it is adventageous to determine the moments of the intensity distribution from only the portion of the image which contains the beam. Including large portions of the image which contain just fluctuations of the background will simply increase the noise level of the calculated moments and make the interpretation of the results more difficult. To achieve all of these goals, the following algorithm was employed: first, each frame was divided into 16-pixel wide vertical and horizontal strips. Along each strip and for each frame of a run, the average pixel value was calculated. Second, the variances (over an entire run) of these averages, separately for each strip, were calculated. These variances are incredibly sensitive for the beam hitting a given strip for even just a few of the 1000 frames of a run. Thus, a simple threshold may be applied to the variances in order to decide whether a given strip should be included in the determination of the moments of the intensity distribution or whether the strip in question should be included in the determination of the average background level.

A run is considered to fully contain the beam if there exists at least one such background strip on the top, bottom, left and right edge of the image. If background strips on one or more of the edges are missing, the run is flagged, since it cannot be guaranteed that the entire beam spot is contained inside all of the frames of a run. The average pixel value of all the background strips is used as an estimate of the average remaining background intensity of the entire image. This value was consistent with zero in case of the 1 μm camera, but it was a significant $1,5 \pm 0,4$ in case of the 2 μm camera, the reason for which is unclear. In any case, this pedestal value was subtracted from all the pixel values which were considered for the calculation of the moments of the intensity distribution. With this algorithm, we have a method in place which allows us (i) to capture the entire beam, and only the beam (and to know when the beam wanders outside the range of the image) and (ii) to subtract the background with sufficient precision.

4. MOMENTS

A Gaussian intensity profile is given by the distribution

$$I(x,y)\mathrm{d}x\mathrm{d}y = \frac{1}{\sqrt{2\pi\sigma^2}} e^{-\frac{x^2}{2\sigma^2}} \mathrm{d}x \frac{1}{\sqrt{2\pi\sigma^2}} e^{-\frac{y^2}{2\sigma^2}} \mathrm{d}y. \tag{1}$$

This distribution can be transformed to planar polar coordinates at which point one obtains

$$I(r,\phi)\mathrm{d}r\mathrm{d}\phi = \frac{r}{\sigma^2} e^{-\frac{r^2}{2\sigma^2}} \mathrm{d}r \frac{1}{2\pi} \mathrm{d}\phi, \tag{2}$$

i.e., a Rayleigh distribution for the radial coordinate r and a uniform distribution for the azimuthal coordinate ϕ. We will see that some observations are not consistent with a radial Rayleigh distribution or a uniform azimuthal

Table 1. Lowest moments of the Rayleigh distribution (radial coordinate), the uniform distribution (azimuthal coordinate from $-\pi$ to π) and contributions from their modifications (see text).

Moments	first	second	third	fourth
Rayleigh	$\sqrt{\frac{\pi\sigma^2}{2}}$	$2\sigma^2$	$3\sigma^2\sqrt{\frac{\pi\sigma^2}{2}}$	$8\sigma^4$
modification	$\times N_\alpha(1+3,75\alpha)$	$\times N_\alpha(1+6\alpha)$	$\times N_\alpha(1+8,75\alpha)$	$\times N_\alpha(1+12\alpha)$
uniform	0	$\frac{\pi^2}{3}$	0	$\frac{\pi^4}{5}$
modification	$-\frac{\beta\sin(2\phi_0)}{2}$	$+\frac{\beta\cos(2\phi_0)}{2}$	$-\frac{\beta\sin(2\phi_0)}{2}(\pi^2-1,5)$	$+\frac{\beta\cos(2\phi_0)}{2}(2\pi^2-3)$

distribution. We will therefore also investigate modifications of these distributions of the form

$$\frac{r}{\sigma^2}e^{-\frac{r^2}{2\sigma^2}}\mathrm{d}r \quad \rightarrow \quad N_\alpha\frac{r}{\sigma^2}\left(1+\alpha\frac{r^4}{4\sigma^4}\right)e^{-\frac{r^2}{2\sigma^2}}\mathrm{d}r, \tag{3}$$

$$\frac{1}{2\pi}\mathrm{d}\phi \quad \rightarrow \quad \frac{1}{2\pi}\left(1+\beta\cos\left[2\left(\phi-\phi_0\right)\right]\right)\mathrm{d}\phi, \tag{4}$$

where the parameters α and β represent small deviations from the unmodified distributions. The parameter ϕ_0 does not need to be small – it gives the angle of the deformation axis of the beam spot relative to the horizontal. Finally we find that $N_\alpha = \frac{1}{1+2\alpha}$ in order to recover a normalized radial distribution (the modified azimuthal distribution remains normalized). We will not compare the observed intensity distributions as such with the model distributions by means of fits or similar. We obtain much more robust quantities by calculating moments of the experimental and model distributions; we will therefore compare those with each other. For this purpose, we list the lowest moments of our model distributions and their modifications in Table 1.

The specific types of modification of the two distributions can be motivated as follows: in case of the radial distribution, a possible lower-order modification of the type $\left(1+\alpha\frac{r^2}{\sigma^2}\right)$ does not produce additions to the moments in first order in α. For such a modification, changes to the moments appear only in second order in α and higher. Another possible modification – by the factor $\left(1+\alpha\frac{r}{\sqrt{\sigma^2}}\right)$ – produces *negative* changes to the moments, which is contrary to the observations. Also, somewhat related to that, if one discusses modifications of a Gaussian beam in planar polar coordinates, one often refers to Laguerre-Gaussian beams. Also in that case, the lowest-order modification of the radial intensity distribution, i.e. by the first non-trivial Laguerre polynomial, produces a term $\propto r^4$ (see for instance Section 4.7.4 in Reference[6]). In the case of the azimuthal distribution, a modification of the type $(1+\cos(\phi-\phi_0))$ would, in fact, shift the centroid of the distribution – hence the modification we employ is the lowest-order modification which does not do that.

5. BEAM WANDER

The first quantity we discuss is beam wander. For this purpose, we calculate for each frame in each run the centerpoint (x, y) of the intensity distribution. For any given run, the averages $(\langle x\rangle, \langle y\rangle)$ are also calculated. In the next step, the differences $(\Delta x, \Delta y) = (x - \langle x\rangle, y - \langle y\rangle)$ are determined for each frame of a run and transformed to planar polar coordinates (r, ϕ) with the origo given by the averages. For each run, we therefore get a sample of one thousand of such coordinate pairs for which we can determine the experimental moments. When comparing these moments to the model predictions (see Table 1), we find that the experimental moments up to fourth order follow the model predictions of the *unmodified* distributions rather well. In the case of the radial distribution, this means that all the four lowest moments can be described in terms of a single parameter σ^2, while the predictions of the lowest four moments of the uniform distributions are parameter-free. We are thus able to model beam wander as a stochastic *Gaussian* process. The remaining task is then to estimate the parameter σ^2 of the radial distribution – preferably as function of the structure constant C_n^2. For this purpose,

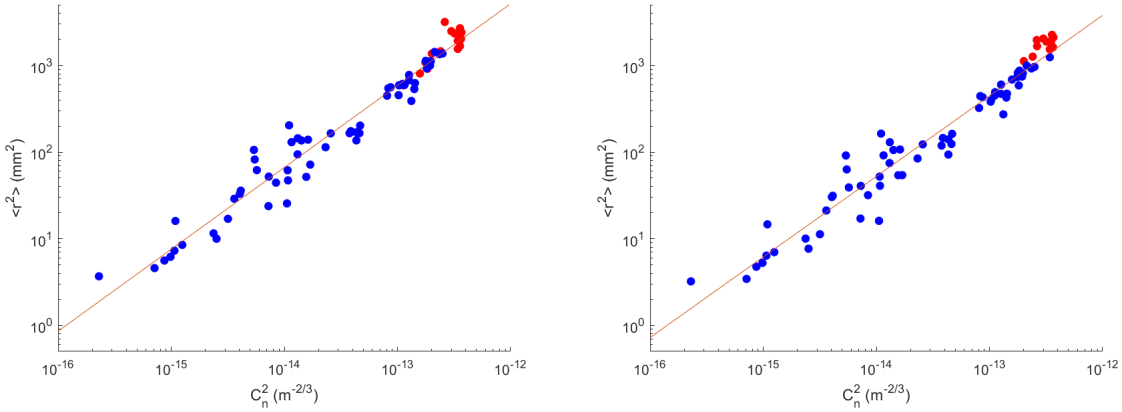

Figure 5. Second moment of the radial distribution $\langle r^2 \rangle$ of the beam wander as function of the structure constant C_n^2 for 1 μm laser light (left) and 2 μm laser light (right). The red dots indicate runs where we cannot guarantee that the entire beam was captured in all the frames of a run. The red line corresponds to a simple fit (see text).

we plot the second moment of the radial distribution $\langle r^2 \rangle$ from each run versus the measured (by ONERAs scintillometer) turbulence level in terms of the structure constant.

We find that on a double-logarithmic plot, the data points center along a straight line. We therefore attempt a simple fit of the data using the fit function

$$\langle r^2 \rangle \ \left[\mathrm{mm}^2\right] = A \left(C_n^2 \ \left[\mathrm{m}^{-\frac{2}{3}}\right] \right)^{\nu} . \tag{5}$$

The fit gives us values in the order of $\nu = 0,95$ and $0,93$ for the 1 μm and 2 μm laser light respectively, i.e., values rather close to a linear relationship between $\langle r^2 \rangle$ and C_n^2 as discussed in, e.g., Section 6.6.2 of the second edition of the book by Andrews and Phillips.[6] If we specifically take Equation (99) from that section (for a focused beam including a finite outer scale), our other fit parameter A translates into an outer scale length in the order of meters for both wavelengths. We can therefore state that the theoretical predictions as discussed in the given reference are consistent with our experimental results for beam wander.

An interesting observation in Figure 5 is that the data (or better the fluctuations of the data around the fit) seem rather similar for both wavelengths. This is partly explained by the fact that data with the same C_n^2 are from the same run, i.e., the two laser beams would therefore have propagated through the exact same turbulent eddies. Still, we were intrigued by the seemingly tight correlation between the fluctuations. We therefore plotted the relative fluctuations in terms of the ratio of the data with the fit function for both wavelengths against each other. The result, as seen in Figure 6, confirms the tight correlation. Fluctuations of up to a factor of three are evident and clearly correlated between the otherwise statistically independent data sets. This means that the fluctuations have a common physical origin in the specific turbulence conditions along the beam path for each run. Here, it is important to remember that the turbulence level C_n^2 for each run was provided by a scintillometer with a beam path a few meters to the side of the laser beam path, and maybe half a meter higher above ground. This means that the scintillometer reading may simply not be entirely representative for the actual turbulence along the laser beam path – differences across the distance may occur. In addition, the type of larger-scale fluctuations responsible for beam wander may simply not produce a representative average during the short times (20 s) of a run. Maybe for longer runs, the specific manifestations of turbulent eddies along the beam path would produce a more representative average and hence give rise to a beam wander $\langle r^2 \rangle$ more in line with the C_n^2 level as measured by the scintillometer (which averages measurements over 60 s). In this context, we would like to remind the reader of the observation on beam wander connected to the video linked in Figure 3. There, we saw a large drift of the beam spot toward the end of the run – a similar excursion might not have been captured with a slightly earlier start time of the run. It is also worth mentioning that, in the course of a day, the beam spot itself would move up by several tens of cm in the morning and early afternoon,

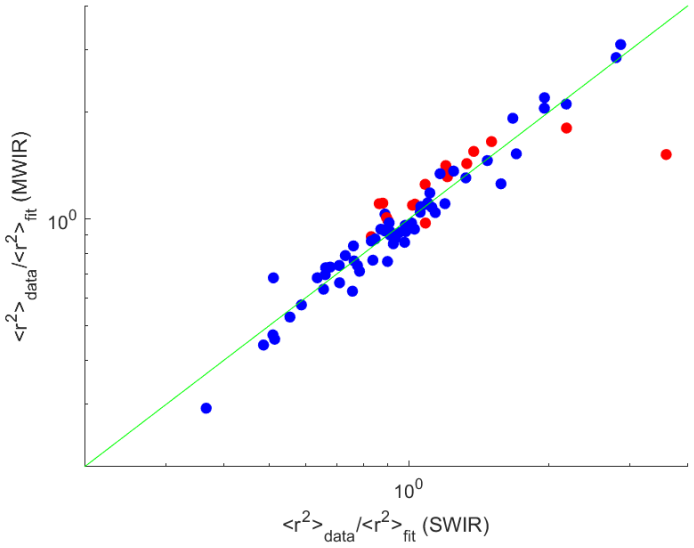

Figure 6. Relative fluctuations (data/fit) of the 2 μm (MWIR) versus the 1 μm (SWIR) beam wander $\langle r^2 \rangle$ per run. Red data points indicate runs where at least one of the laser beams is not guaranteed to be captured inside all the frames of a run. Fluctuations are tightly correlated with each other, pointing to a common, physical origin. For possible interpretations, see text.

while it would move down again during the remaining afternoon and early evening. This diurnal movement was counteracted by angling the laser head by a fraction of a mrad each time. The cause for this slow, large-scale wander of the beam spot is of course the development and disappearance of an average (negative) temperature gradient in the air above ground due to the daily solar radiation cycle. Considering such type of beam wander, it might be doubtful that a representative sampling of beam wander considerably can be achieved within any reasonable time span over which turbulence may be characterized by a single C_n^2.

In this context, it is now also interesting to investigate the temporal aspect of beam wander, i.e., its time series and their Fourier transforms. We therefore compute the correlation function

$$R_x(\tau) = \frac{\int \Delta x_1(t+\tau)\Delta x_2(t)\mathrm{d}t}{\sqrt{\int \Delta x_1^2(t)\mathrm{d}t \times \int \Delta x_2^2(t)\mathrm{d}t}}, \tag{6}$$

which becomes the autocorrelation function in the case of $x_1 = x_2$. Unfortunately, a design error of the experiment became apparent when investigating the correlation function. Instead of recording time stamps with ms accuracy for every frame, we relied on the fact that the cameras were supposedly recording frames at a 100 Hz rate. Together with the 50 Hz laser pulses, this should have resulted in a 50 Hz rate of background subtracted frames, i.e., a time series with a consistent 20 ms difference between frames. While the 2 μm camera, as far as we can tell, was able to record reliably at this rate, the 1 μm camera dropped about 1 in 60 frames in an apparently random fashion, such that its time series contains holes in the sense that 1 in 60 time differences between frames are in fact 40 ms and not the expected 20 ms. This does not affect the autocorrelation function all that much, however the correlation between the time series of the two cameras is destroyed – it does not peak at $\tau = 0$ and it is artificially widened by the ever increasing mismatch in time. We will therefore only discuss the autocorrelation functions.

Figure 7 shows the autocorrelation functions R_x and R_y separately, as function of frame-number difference. In the case of the 2 μm laser beam, the frame-number difference translates to a time difference according to $\tau = \Delta N \times 20$ ms. This is also approximately correct for the 1 μm laser beam despite the dropped frames. Since the autocorrelation functions from any given run are rather noisy, we present the average functions over all 76

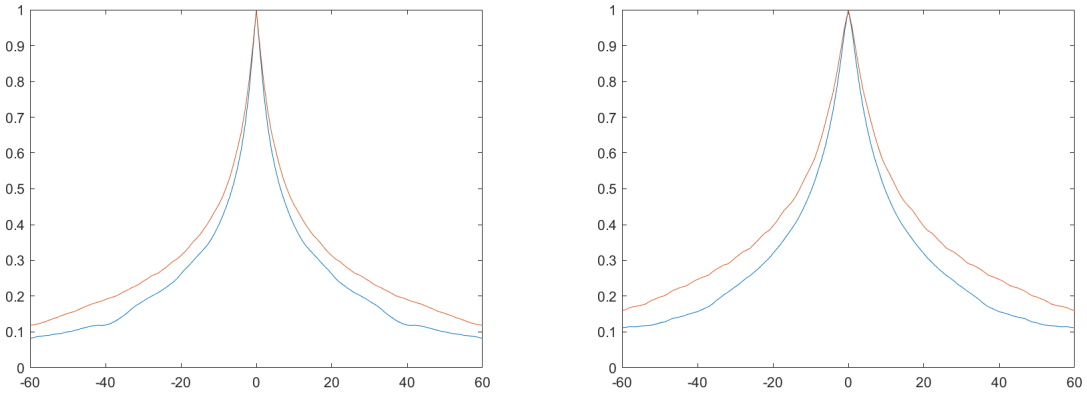

Figure 7. Autocorrelation of the beam wander time series Δx (blue curves) and Δy (red curves) as function of frame-number difference for the 1 μm laser beam (left) and the 2 μm laser beam (right) averaged over all runs. A similar correlation between the two time series of both beams could not be produced, since it turned out that the 1 μm camera dropped about 1 in 60 frames in an apparently random fashion (see text).

runs, which also means that these functions correspond to an average over all turbulence conditions and wind speeds we have encountered during the trial. All four autocorrelation functions look somewhat similar with a rather steep decline from the center up to a frame-number difference of about $\Delta N = \pm 15$ translating to a time difference of some 0,3 s, while the decline becomes more gradual for larger time differences. Interestingly the autocorrelation function R_y (red) lies consistently above R_x (blue), especially for large time differences, indicating that temporal correlations of beam wander in the vertical direction are more persistent than those in horizontal direction. Physically, in the first meter above ground, the development of a stable average vertical temperature gradient due to solar irradiation together with the fact that the wind will blow necessarily more in a horizontal than vertical direction might be responsible for this observation.

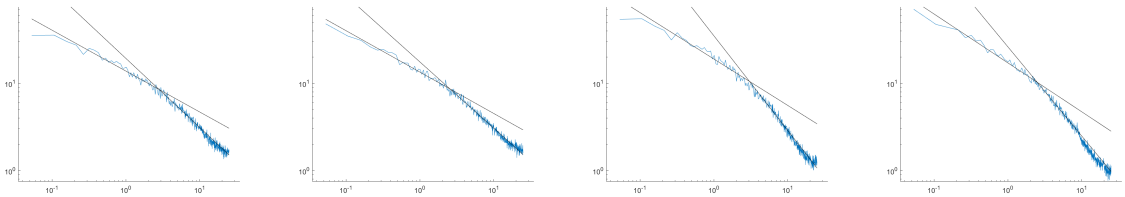

Figure 8. Fourier transforms of the time series according to Equation (7). The four panels show (in this order) the results for the x and y directions for the 1 μm laser beam and similar for the 2 μm laser beam. On the vertical axis, the units are for convenience pixel numbers, while the horizontal axis is the usual frequency in [Hz]. The straight lines are fits to the specific frequency regions (see text)

Similar observations can be made by looking at the Fourier transforms of the time series according to

$$\xi(f_x) = \frac{1}{\Delta t} \left| \int [x(t) - \bar{x}]\, e^{-2\pi i f_x t} \mathrm{d}t \right|, \tag{7}$$

and similar for the y direction. Figure 8 shows the corresponding results on double-logarithmic plots. We have tried to fit the regions 0,1–2,7 Hz and 4–9 Hz in all the four plots by straight lines and found that the lower frequency region produces a slope of -0,5 indicating a $1/\sqrt{f}$ dependence, while the higher frequency region produces a slope in the order of -0,8 to -1 for the 1 μm and 2 μm laser beam, respectively, indicating a dependence closer to $1/f$. The transition region lies in the range of 2,5–3 Hz, which confirms the observation of a similar transition apparent in the time domain by the autocorrelation function around $\Delta t = 0,3$ s. Also interesting is

that the lowest-frequency data points in case of the x direction (first and third panel) start to deviate from the $1/\sqrt{f}$ dependence, while this is not evident for the y direction. Also this is in line with the previous observation that correlations in y direction are more persistent than those in x direction.

6. LONG- AND SHORT-TERM SPOT

We start the discussion of the beam spots with the characterization of the short-term beam spot. Short term in this context means averaging over the shutter time (< 1 ms). Experimentally, since we already had the centerpoints (x, y) of the intensity distribution from each frame (see Section 5), the easiest way to proceed was to determine the radial and azimuthal moments of the intensity distribution for each frame with respect to this centerpoint and then to average the results over an entire run. Mathematically, this should produce the same values as shifting all the single intensity distributions of a run to the same centerpoint, for then to calculate the moments from the summed intensity distribution – provided that the recorded intensity per frame is identical, which we confirmed was approximately true. However, the resulting moments did not conform to the moments of the unmodified model distributions discussed in Section 4. This, in fact, prompted us to investigate the modified model distributions.

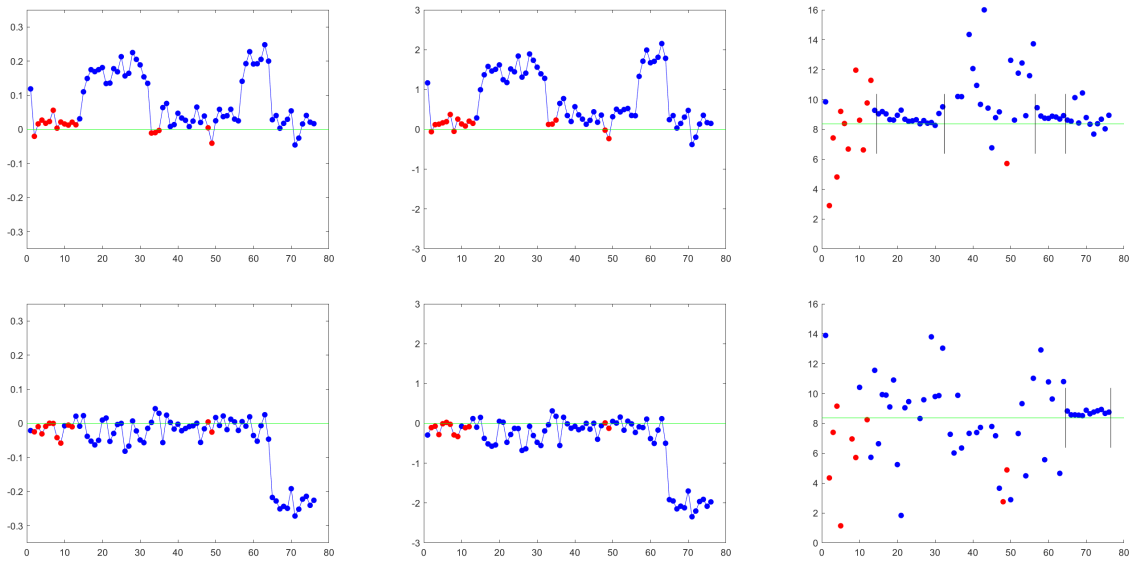

Figure 9. From left to right: first moment $\langle\phi\rangle$, third moment $\langle\phi^3\rangle$, and their ratio $\langle\phi^3\rangle/\langle\phi\rangle$ of the azimuthal intensity distribution of the 1 μm short-term laser beam spot (upper row) and correspondingly for the 2 μm short-term laser beam spot (lower row) for all the 76 runs. The green, horizontal lines correspond to expectations from the model distributions, the black, vertical lines indicate regions, which will be discussed further (see text). Red dots again indicate runs, where it is not guaranteed that the entire beam is captured in all the frames of a run.

Figure 9 shows the experimental moments $\langle\phi\rangle$ and $\langle\phi^3\rangle$ for the short-term beam spots of all the runs and both wavelengths. From Table 1, we know that for a uniform azimuthal distribution, these moments are expected to be zero. This is evidently not true for all the runs. We therefore try to explain the observations with the modified azimuthal distribution discussed in Section 4. This modified distribution allows for non-zero odd moments. The most relevant prediction of this distribution, however, is the ratio of the third with the first moment, which according to Table 1 should be equal to $\pi^2 - 1,5 \approx 8,4$. This is a parameter-free and hence very robust prediction, which we can test experimentally. Indeed, for those runs, where the odd moments depart from zero (marked by the vertical black lines in the rightmost panels), the ratios of these moments adhere very well to the value predicted by this model, which means that the model distribution most likely captures the essential deviation of the experimental distribution from a uniform distribution.

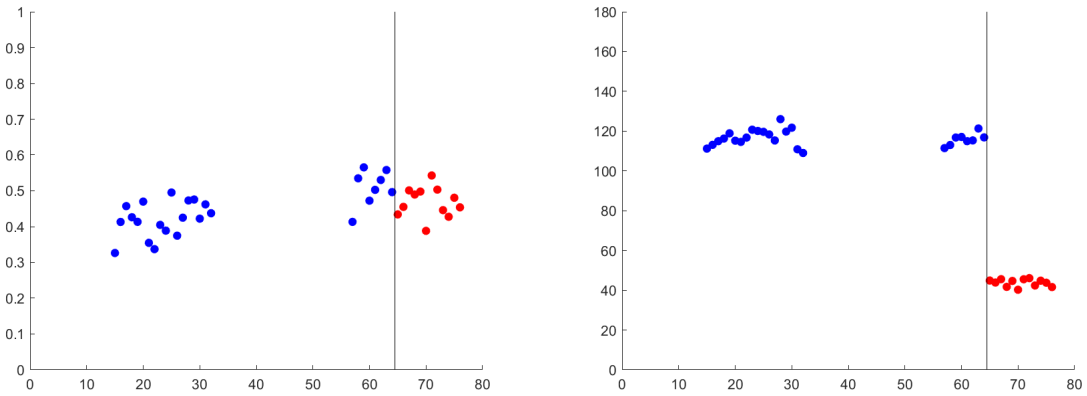

Figure 10. Left panel: parameter β (the degree of quadrupole asymmetry) of the modified azimuthal distribution as calculated by Equation (8) for those runs, where the modified azimuthal distribution describes the experimental moments. Right panel: parameter ϕ_0 (the deformation direction of the asymmetry in degrees) as calculated by Equation (9) for the same runs. Blue dots indicate data from the 1 μm laser beam spot, red dots those from the 2 μm laser. The vertical line indicates the point in time during the trial where the oblong shape of the 1 μm laser beam spot was discovered and fixed by adjusting the optics in the laser head (see Figure 2). The resulting oblong shape of the 2 μm spot was first discovered in the offline analysis.

Encouraged by this, we can even try to extract the two parameters of the modified azimuthal distribution by calculating

$$\beta = 2\sqrt{\langle\phi\rangle^2 + \left(\langle\phi^2\rangle - \frac{\pi^2}{3}\right)^2}, \tag{8}$$

$$\phi_0 = \frac{1}{2}\arctan\left[-\frac{\langle\phi\rangle}{\langle\phi^2\rangle - \frac{\pi^2}{3}}\right], \tag{9}$$

i.e. two suitable combinations of the first and second moments of the experimental distributions. Figure 10 shows the results of these calculations for those runs, where the modified azimuthal distribution is needed to describe the experimental moments. One can see that calculations produce a consistent, rather sizeable parameter β responsible for the oblong shape of the beam spot. When the oblong shape of the 1 μm laser beam spot was discovered (at the end of run 64 during the evening of Oct. 13 under low turbulence conditions), the optics in the laser head was adjusted. This fixed the oblong shape of the 1 μm laser beam spot, however, it probably caused a similar oblong distortion of the 2 μm laser beam spot to appear. Interestingly, the axis of deformation of the 2 μm laser beam spot turned out to be almost perpendicular to the previous one of the 1 μm spot, as evident from the data in Figure 10. It is not clear what caused the oblong shape to begin with and why it disappeared by itself after run 32 for then to reappear again at run 57 – at least it is not caused by atmospheric turbulence. However, it shows how moments of the intensity distribution can be used for beam diagnostics, even though the beam passes through 1 km of turbulent atmosphere. We are therefore encouraged to use moments of also the radial distribution to further characterize the shape of the beam spot.

When comparing the experimental moments to those of a radial model distribution, e.g., the Rayleigh distribution, we have to keep in mind that even the unmodfied model distribution contains one free parameter σ^2, meaning that the predicted moments are not parameter-free as it was the case for the uniform angular distribution. In order to produce parameter-free predictions, we therefore have to compare ratios of moments of the form $\sqrt[n]{\frac{\langle r^n\rangle}{\langle r\rangle^n}}$. The values of these ratios can be deduced from the results shown in Table 1, however, for convenience, we will list these ratios, both for the unmodified (Rayleigh) distribution as well as for the modified radial distribution (up to first order in the parameter α) in Table 2. The comparison of ratios of experimental moments with those from the model distributions reveals that the moments of the radial intensity distribution of

Table 2. Ratios of the type $\sqrt[n]{\frac{\langle r^n\rangle}{\langle r\rangle^n}}$ for the moments of the Rayleigh distribuion and the modified radial distribution (up to first order in α) as discussed in Section 4. For more details, see text.

Ratios for $n=$	2	3	4
Rayleigh	$\frac{2}{\sqrt{\pi}}$	$\sqrt[3]{\frac{6}{\pi}}$	$2\frac{\sqrt[4]{2}}{\sqrt{\pi}}$
modification	$\times(1+0,25\alpha)$	$\times(1+0,5\alpha)$	$\times(1+0,75\alpha)$

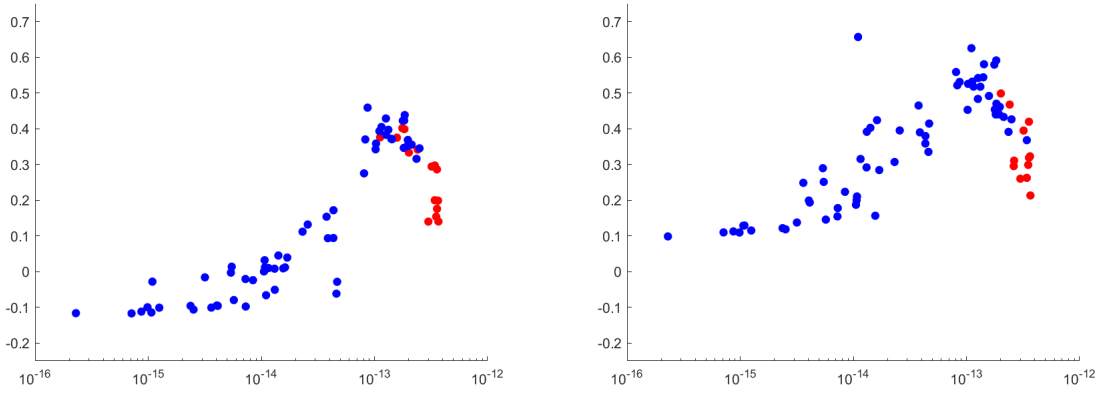

Figure 11. Left panel: value of parameter α required to reproduce the experimental moment ratios by the model distribution (see Table 2) for the 1 μm short-term beam spot as function of turbulence level given by the structure constant C_n^2. Right panel: similar for the 2 μm short-term beam spot. Red dots are from runs where we cannot guarantee that the intensity distribution is captured in all the frames of a given run.

the short-term beam spot cannot be described by the Rayleigh distribution, except for maybe under the weakest turbulence conditions as characterized by the C_n^2 values. The agreement between moment ratios from experiment and model distribution becomes much better for the modified radial distribution as discussed in Section 4. This is of course not that surprising, since the introduction of a further, free parameter α in the model (indicating a wider tail of the distribution) is generally expected to improve the agreement with experiment. What makes us confident that this second parameter captures some physical effect is that it varies systematically with turbulence level as shown in Figure 11. There, we show for each run the value of α which is required to bring the three ratios $\sqrt[n]{\frac{\langle r^n\rangle}{\langle r\rangle^n}}$ for $n=2\ldots4$ of the modified radial distribution in best agreement with experiment. We can see that for the lowest turbulence levels (10^{-15}–10^{-14} m$^{-2/3}$) α is around $-0,1$ and $+0,1$ for the 1 μm and 2 μm short term beam spots, respectively (the deviation by $\pm0,1$ from the expected value of 0 is probably indicative of the systematic uncertainty, i.e. the quality of the data). From $C_n^2=10^{-14}$ m$^{-2/3}$ and onward to higher turbulence levels, the value of the parameter α increases, indicating an increasing deviation of the radial distribution from a Rayleigh distribution. The red dots in Figure 11 indicate runs where we cannot guarantee that the entire intensity distribution is captured in all the frames of a run, hence, their deviation from the general trend should not be worrisome. The deviation of the experimental radial distribution from a Rayleigh distribution should not surprise us, when looking back at the videos linked in Figures 3 and 4. The videos of runs under high turbulence conditions show clear departure of the short-term beam spots from a Gaussian shape. In fact, in many of these frames a break-up of the beam spot into two or more spotlets is evident. Under such circumstances, it is in fact surprising that the experimental moments do not show a larger deviation from the Rayleigh moments. In this context, we should probably emphasize that the discussion of the deviation from a Gaussian beam-spot shape in terms of the parameter α is entirely independent of the other parameter σ^2 which indicates the size of the (residual Gaussian) beam spot size and its increase with turbulence level. So what we have discussed so far

is the increasing *departure* from a Gaussian shape, not the *general increase* of the beam spot with turbulence level. We should also mention that the modification of the radial distribution we have proposed in this work is an entirely phenomenological modification, somewhat motivated by the theory of Laguerre-Gauss beams. Other modifications such as an $e^{-\alpha \frac{r}{\sqrt{\sigma^2}}}$ term with a linear dependence on r in the exponent could also be discussed. Based on the current data, we have not been able to find experimental evidence which allows us to prefer one type of modification over the other.

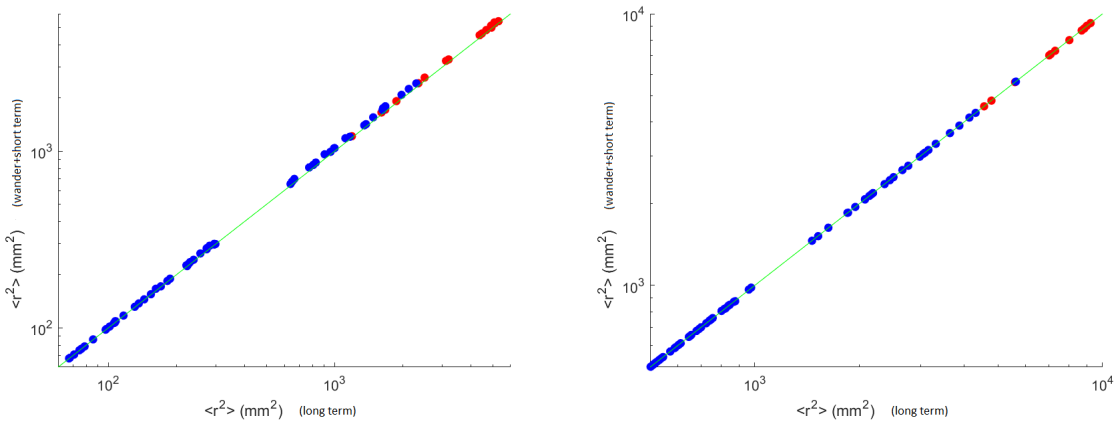

Figure 12. Sums of second moments $\langle r^2 \rangle$ from beam wander and the radial intensity distribution of the short-term beam spot versus the second moment of the radial intensity distribution of the long-term beam spot for the 1 μm laser (left) and the 2 μm laser (right) for each run. If beam wander and short-term beam spot size contribute statistically independently to the long-term beam spot size, the data should line up along the diagonal (marked by the green line). Red dots are from runs where we cannot guarantee that the entire intensity distribution is captured in all the frames of a run.

For the remainder of this section, we will discuss beam spot sizes (both long-term and short-term) and their increase with turbulence level. For the purpose of the short-term beam spot size, we recur to the second moments $\langle r^2 \rangle$ from the analysis discussed so far in this section. For analyzing the long-term beam spot, we simply added all the frames of a run on top of each other and calculated moments (for ϕ and r) of the resulting intensity distribution. Out of these moments, we will only discuss the second moment of the radial distribution in this work. The other moments showed effects reminiscent of the effects which we have already discussed in the context of the short-term beam spot, however, the effects on the long-term beam spot are much less clear or significant, since they are overshadowed by the additional effect of beam wander. This brings us straight to the question to what degree the effects of beam wander and short-term beam spot increase can be treated as independent contributions to the long-term beam spot increase. For this purpose, we have plotted in Figure 12 the sums of the two $\langle r^2 \rangle$ contributions from beam wander (from Figur 5) and short-term beam spot (from Figure 14) versus the single $\langle r^2 \rangle$ values from the long-term beam spot (from Figure 13) for each run. For statistically independent quantities, the variances should simply add up, which means that the datapoints in Figure 12 should all line up along the diagonal, i.e. the green line. That the experimental points conform to this expectation allows us to treat both processes (beam wander and short-term beam widening) as statistically independent from each other. Since we already have shown that beam wander can be described as a stochastic Gaussian process, we can now go even one step further and describe it as a stochastic Gaussian process independent on short-term beam widening processes.

This brings us finally to the discussion of beam-spot sizes as function of turbulence level. Figure 13 shows the second moment of the radial long-term intensity distribution as function of turbulence level. Long term in this context means averaging over one run, i.e. 20 s. At the start of the experiment, we tried to focus both laser beams on the target by adjusting the optics in the laser head such that the beam spots for both laser beams were minimized. Our hope was therefore that under minimal turbulence conditions, the beam spot size was diffraction-limited. At this point, we would like to remind the reader that the second moment of a Gaussian intensity distribution relates according to $\langle r^2 \rangle = \frac{1}{2} W^2$ to the more common $1/e^2$ beam radius W. Furthermore,

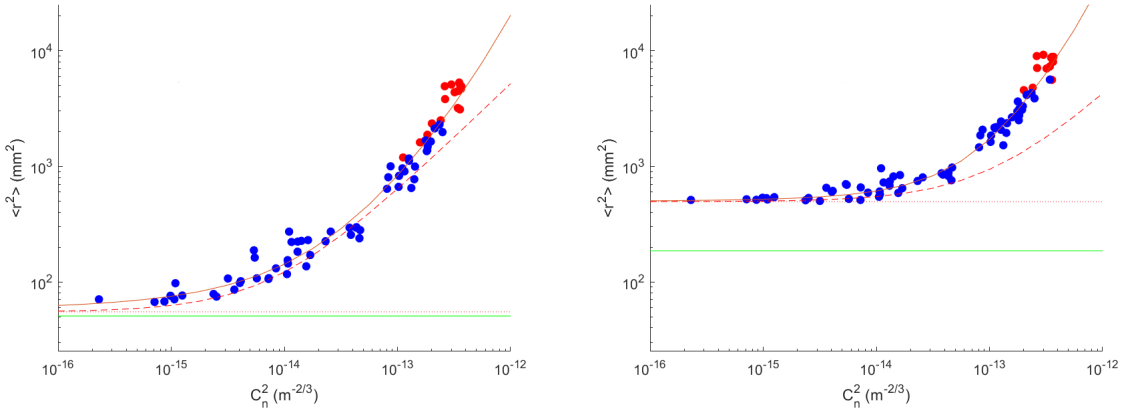

Figure 13. Long term beam spot size in terms of $\langle r^2 \rangle$ as function of turbulence level for the 1 μm laser (left) and 2 μm laser (right) beam. Red dots indicate runs for which we cannot guarantee that the entire intensity distribution is captured in all the frames of a run. The green lines indicate the diffraction limit, while the red dotted lines indicate the presumed beam spot size in the absence of turbulence. The dashed curves include the added contributions to the dotted lines from beam wander (see Figure 5); the solid curves are fits to the data (see text).

the beam radius at the focal distance F_0 is given by $W = \frac{F_0 \lambda}{\pi W_0}$, where W_0 is the beam radius at the aperture. In our case, this gives beam radii at the target of some 1 cm and 2 cm for the two wavelengths, translating to lower $\langle r^2 \rangle$ limits in the order of 50 mm^2 and 200 mm^2, respectively. These limits are marked off as green lines in Figure 13 (and Figure 14 for that matter), where one can see that this limit is never reached by the 2 μm laser beam. This means that we were not able to properly focus the 2 μm laser beam on the target. An alternative explanation – that the beam quality was much different from $M^2 = 1$ – can be ruled out on the grounds that we used a single-mode fiber laser. Therefore, in order to describe the widening of the long-term beam spot with turbulence we had to subtract not the diffraction-limited spot size, but a value which we deemed equal to the presumed spot size in the absence of turbulence. We chose $\langle r_0^2 \rangle$ values of 55 mm^2 and 495 mm^2 for the 1 μm and 2 μm laser beams, respectively, where the first value is barely larger than the diffraction limit. Since plotting values of $\langle r^2 \rangle - \langle r_0^2 \rangle$ versus values of C_n^2 did not produce straight lines, neither on linear nor on logarithmic plots, we finally tried to plot values of $\log \left[\langle r^2 \rangle - \langle r_0^2 \rangle \right]$ versus values of C_n^2 which did produce straight lines on a double-logarithmic plot. Hence, we found a rather simple fit function of the type

$$\left(\langle r^2 \rangle - \langle r_0^2 \rangle \right) \ \left[\mathrm{mm}^2 \right] = \exp \left\{ B \left(C_n^2 \ \left[\mathrm{m}^{-\frac{2}{3}} \right] \right)^m \right\}, \tag{10}$$

with two fit parameters B and m (the value of $\langle r_0^2 \rangle$ was fixed before attempting the fit). The fit produced consistent values of $m = 0,17$ and $B = 1,2\text{–}1,3 \times 10^3$ for both wavelengths. The fits are shown as solid red curves in Figure 13.

Beside the fits to the data, we also show the added contributions of beam wander (the dashed red lines) in Figure 13. Since we by now know that the variances from beam wander and short-term beam spot size are additive, we have generated – by fitting both the long-term beam spot size and the beam wander variance – at the same time a description of the short-term beam spot size as function of turbulence level. For this, we simply have to subtract the results of Equation (5) from the results of Equation (10). This gives precisely the red solid curves in Figure 14 where we can observe that they describe the short-term beam spot size in a satisfying manner. Again, the green and red horizontal lines are the diffraction limit and the presumed beam-spot size in absence of turbulence, respectively. Altogether, we have managed to achieve a description of the long-term beam spot size and its two statistically independent contributions – beam wander and short-term beam spot size – as function of turbulence level on the basis of four free fit parameters (yielding similar values for the two wavelengths) and one parameter $\langle r_0^2 \rangle$ modelling the beam spot size in the absence of turbulence. This last parameter might be replaced by the theoretical diffraction limit in the case, a good focus on the target is achieved.

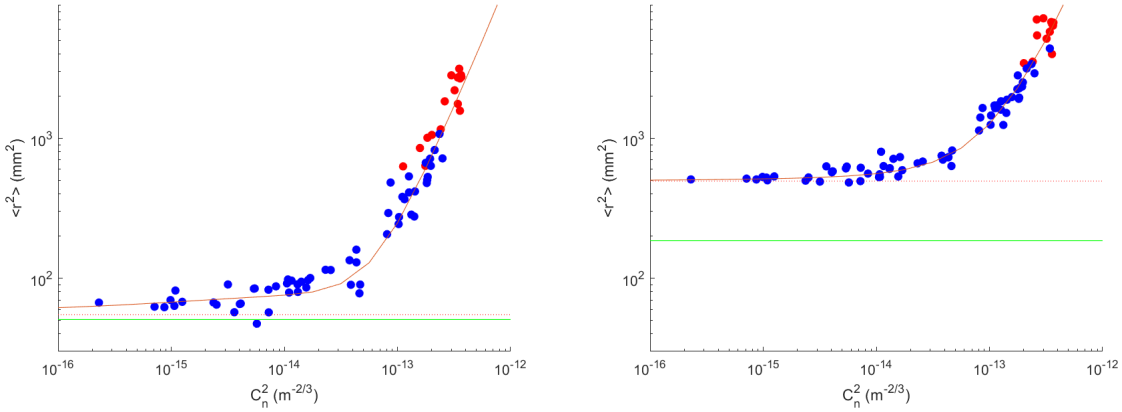

Figure 14. Short term beam spot size in terms of $\langle r^2 \rangle$ as function of turbulence level for the 1 μm laser (left) and 2 μm laser (right) beam. Red dots indicate runs for which we cannot guarantee that the entire intensity distribution is captured in all the frames of a run. The green lines indicate the respective diffraction limits, while the red dotted lines indicate the presumed beam spot sizes in absence of turbulence. The solid curves are the differences between the fits to the long-term beam spot data (see Figure 13) and the beam wander data (see Figure 5). The agreement is satisfying.

7. CONCLUSION AND OUTLOOK

In summary, we have conducted an experiment on laser-beam propagation through turbulent atmosphere. For this, we have produced two laser beams of 1 μm and 2 μm wavelength with a common beam axis. These beams were propagated along a 1 km path, roughly 1 m above ground onto a target which was observed by two cameras at a few meters distance. The main goal of the experiment was to gain experience with laser propagation through turbulent atmosphere such that we are better prepared to develop a strategy for how to deliver sufficient effect on a given spot of a potentially fast moving target for it to take damage. One important part of the experiment was therefore to characterize the beam spot in terms of size and shape to be able to judge the quality of the focus which we were able to achieve in the field. It turned out that we were only able to produce a good focus with a round beam for some of the runs with the 1 μm laser beam. In terms of area, the smallest beam spot which we could achieve with the 2 μm beam was 2,5 times the diffraction limit. The shape of the 1 μm beam showed an angular asymmetry for many of the runs, which, when adressed by adjusting the optics, made the 2 μm beam turn asymmetric instead. All of these things are of course a field for improvements in the future.

Despite these problems, we were able to extract data on beam wander, long-term (averaged over 20 s) beam spot size and short-term (within the shutter time of < 1 ms) beam spot size as function of turbulence level. Since we were not planning on addressing specific problems regarding the theoretical modelling of optical turbulence or questions relating to simulations of laser propagation, we keep the description of our findings mainly on a rather phenomenological level. Specifically, we find that beam wander can be treated as a stochastic Gaussian process independent on short-term beam widening processes. Moreover, the variance of beam wander is consistent with a linear dependence on C_n^2 and in general agreement with the theoretical description provided in Section 6.6.2 of Reference.[6] From the autocorrelation function and the Fourier transformations of the beam-wander time series, we find that its frequency content follows roughly a $f^{-1/2}$ law for frequencies less than 2,5–3 Hz, and a f^{-1} law for frequencies larger than that. This analysis is based on averages over all turbulence conditions and should be repeated with more data, longer time series and shorter time intervals between frames, in order to produce results separated for different turbulence condidtions as well as for smaller and larger frequencies than what we have investigated so far. The present information is, however, already useful for dimensioning a tip-tilt mechanism which – besides for fine-tracking of a target – may be used for counteracting the effect of beam wander. Due to an experimental problem – the 1 μm camera dropped about 1 in 60 frames in a random fashion – it was not possible to obtain the correlation function between the beam-wander time series of the two laser beams. By adding time stamps with ms resolution to each frame, this problem may be circumvented in future experiments.

The analysis of the long-term and short-term beam spot sizes suffered from unsatisfactory focusing of the

beam. We have therefore investigated the increase of the beam spot area over its presumed size in the absence of turbulence, i.e., $\langle r^2 \rangle - \langle r_0^2 \rangle$, where, in particular for the case of the 2 μm beam, the parameter $\langle r_0^2 \rangle$ was much larger than given by the theoretical diffraction limit. This increase in beam size as function of turbulence level could be described by a two-parameter fit with quite similar parameter values for the two laser beams. Moreover, besides describing the long-term spot size, the fit minus the fit to the beam-wander variances gives also a good description of the short-term spot size as function of turbulence level. No attempt has been made to compare the spot-size data or the fit to theoretical model descriptions or results from simulations.

ACKNOWLEDGMENTS

We would like to thank ONERA – The French Aerospace Lab – and their staff for organizing the field trial and for help and support during the measurements at their Fauga-Mauzac site. We would also like to thank L.G. Holmen for producing the video sequences from the single frames.

REFERENCES

[1] Space Optics Research Labs, LLC, "Beam Expanders – COAR Series." http://sorl.com/portal25/index.php/products/coar-series. (Accessed: 7 August 2023).

[2] Lippert, E., "Safety assessment of laser propagation set-up." FFI-notat 22/01730 (2022).

[3] National Instruments CORP, "CompactRIO Systems." https://www.ni.com/en-no/shop/compactrio.html. (Accessed: 7 August 2023).

[4] Sensors Unlimited (a Collins Aerospace Company), "SWIR area Cameras." https://www.sensorsinc.com/products/area-cameras/. (Accessed: 7 August 2023).

[5] Teledyne FLIR, "High performance Cameras." https://www.flir.eu/browse/rampd-and-science/high-performance-cameras/? (Accessed: 7 August 2023).

[6] Andrews, L. C. and Phillips, R. L., [*Laser Beam Propagation through Random Media*], SPIE Press, Bellingham, WA (2005 (second edition)).